

Magnetorotational instability in eccentric disks under vertical gravity

Chi-Ho Chan¹, Tsvi Piran², and Julian H. Krolik³

¹Center for Relativistic Astrophysics and School of Physics, Georgia Institute of Technology, Atlanta, GA 30332, USA

²Racah Institute of Physics, Hebrew University of Jerusalem, Jerusalem 91904, Israel

³Department of Physics and Astronomy, Johns Hopkins University, Baltimore, MD 21218, USA

December 10, 2023

ABSTRACT

Previously we demonstrated that the magnetorotational instability (MRI) grows vigorously in eccentric disks, much as it does in circular disks, and we investigated the nonlinear development of the eccentric MRI without vertical gravity. Here we explore how vertical gravity influences the magnetohydrodynamic (MHD) turbulence stirred by the eccentric MRI. Similar to eccentric disks without vertical gravity, the ratio of Maxwell stress to pressure, or the Shakura–Sunyaev α parameter, remains $\sim 10^{-2}$, and the local sign flip in the Maxwell stress persists. Vertical gravity also introduces two new effects. Strong vertical compression near pericenter amplifies reconnection and dissipation, weakening the magnetic field. Angular momentum transport by MHD stresses broadens the mass distribution over eccentricity at much faster rates than without vertical gravity; as a result, spatial distributions of mass and eccentricity can be substantially modified in just ~ 5 to 10 orbits. MHD stresses in the eccentric debris of tidal disruption events may power emission ≥ 1 yr after disruption.

Unified Astronomy Thesaurus concepts: Magnetohydrodynamical simulations (1966); Accretion (14); Black hole physics (159); Gravitation (661)

1. INTRODUCTION

Much has been learned about the dynamics of disks whose material travels on circular orbits. In disks with enough ionization to support electrical conductivity, the internal stress transporting angular momentum outward and allowing material to drift inward is primarily magnetic: The fast-growing magnetorotational instability (MRI) stirs up magnetohydrodynamic (MHD) turbulence, and orbital shear correlates the radial and azimuthal components of the turbulent magnetic field to produce this stress (Balbus & Hawley 1991, 1998; Hawley & Balbus 1991). The nonlinear development of the MRI has been extensively explored, both in shearing-box and global-disk settings (e.g., most recently, Wissing et al. 2022; Zier & Springel 2022; Sandoval et al. 2023; Jacquemin-Ide et al. 2023).

However, disks might also be eccentric. One common cause is external gravitational perturbation: Disks acquire forced and free eccentricities as a result of secular gravitational interaction with eccentric binaries (e.g., Murray & Dermott 1999), and nonaxisymmetric components of gravity resonantly amplify small initial eccentricities (Whitehurst 1988; Lubow 1991). Internal processes such as viscous overstability (Kato 1978; Lyubarskij et al. 1994; Ogilvie 2001) can also give rise to eccentricity. Alternatively, disks can be created eccentric in multiple ways: outgassing from planetesimals (Trevascus et al. 2021), or tidal disruption of stars (Shiokawa et al. 2015; Piran et al. 2015; Svirski et al. 2017) and molecular clouds (e.g., Bonnell & Rice 2008) by supermassive black holes. There is observational evidence for eccentric disks as well, such as asymmetric lines in white dwarfs (e.g., Gänsicke et al. 2006), and asymmetric broad emission lines in active galactic nuclei (e.g., Eracleous et al. 1995; Tucker et al. 2021) and tidal disruption events (TDEs) (e.g., Guillochon et al. 2014; Liu et al. 2017).

In magnetized eccentric disks, MHD stresses likely outcom-

pete hydrodynamic forces in directing disk evolution. Analytic treatment of stresses in eccentric disks (Ogilvie 2001; Lynch & Ogilvie 2021a,b) is limited in applicability because the prescriptions it relies on, even when applied to circular disks, may not adequately represent the nature of turbulent MHD stresses pumped by the MRI. Recent years have seen exploration of the MRI in eccentric disks. The studies published so far all assume unstratified disks, that is, disks unaffected by vertical gravity. Chan et al. (2018) showed analytically that the MRI is a robust instability that continues to be active up to extremely high eccentricities. Chan et al. (2022) conducted MHD simulations to examine how the variation of orbital properties around the disk affects the nonlinear evolution of the MRI in moderately eccentric disks. These simulations revealed that the MRI develops much like in circular disks, but with noticeable local departures. Interestingly, the simulations of Dewberry et al. (2020) suggested that sharp changes of eccentricity or orientation over radius may suppress the MRI.

This article investigates the behavior of the eccentric MRI in disks subject to vertical gravity, also known as stratified disks. Vertical gravity affects eccentric disks in ways not possible in circular disks. As material in an eccentric disk moves closer and farther away from the central object, vertical gravity strengthens and weakens, and the disk collapses and puffs up accordingly. Vertical gravity varies on the orbital timescale, which is comparable to the vertical sound-crossing timescale, so the disk is never in vertical force balance. The amplitude of this vertical disk breathing can be quite large even at moderate eccentricities (Ogilvie & Barker 2014; Ryu et al. 2021; but see Lynch & Ogilvie 2021b). Three-dimensional effects can manifest themselves hydrodynamically (Ogilvie 2008; Teyssandier & Ogilvie 2016; Ryu et al. 2021); as we shall show here, MHD effects can be considerably stronger.

Our previous unstratified simulations (Chan et al. 2022) were

novel in that, although their dynamics were purely Newtonian, they took advantage of the coordinate flexibility afforded by a general-relativistic (GR) formulation to implement a coordinate system tailored to the eccentric disk shape. Here we build on that framework: The strong height modulation makes an unstratified disk challenging to resolve with traditional grids, so we generalize the method to devise a customized grid with variable cell height.

We explain our calculational approach in Section 2; a high-level synopsis is given in Section 2.1. Our results are collected in Section 3, prefaced by a summary of key findings in Section 3.1. We discuss these results in Section 4 and conclude in Section 5.

2. METHODS

2.1. Overview

We study the nonlinear development of the MRI in a stratified disk with a moderate eccentricity that is uniform across the disk. This work extends the unstratified simulations in Chan et al. (2022) by adding vertical gravity. The disk height responds to the varying vertical gravity along the orbit; our goal is to see how this disk breathing influences MHD turbulence. For a uniformly eccentric disk, midplane orbits are divergence-free and surface density is constant along any orbit; the lack of horizontal compression makes this kind of disk useful for isolating the effects of vertical gravity.

It is instructive to situate our disk in the context of previous studies of eccentric disks. Two fundamental characteristics of an eccentric disk are its eccentricity and aspect ratio, the latter being the ratio of vertical scale height to orbital length scale. Our disk is moderately eccentric and geometrically thin, resembling those studied analytically by, e.g., Ogilvie & Barker (2014). Ryu et al. (2021) found that vertical gravity promotes shocks in the case of high eccentricity and large geometrical thickness, but neither criterion for shocks is satisfied in our disk.

We assume the gas is adiabatic with an adiabatic index of $\gamma = \frac{5}{3}$, in contrast to the almost isothermal equation of state used in Chan et al. (2022). A stiffer equation of state reduces the degree of disk breathing, making the problem more numerically tractable, but has little effect on the character of MHD turbulence. We also assume that ideal MHD applies.

Despite the Newtonian nature of the problem, we follow Chan et al. (2022) and adopt a general-relativistic magnetohydrodynamics (GRMHD) formulation so we can use the coordinate freedom that comes with it to make our grid better match the geometry of a stratified eccentric disk. One reason we employ the finite-volume GRMHD code Athena++ (White et al. 2016; Stone et al. 2020) is that it readily supports arbitrary coordinate systems. In keeping with GR tradition, we adopt gravitational units, that is, the central mass M is unity, velocities are in terms of the speed of light c , and lengths are in gravitational radii GM/c^2 .

As Chan et al. (2022) argued, the balance between the competing desires to have Newtonian dynamics and to limit truncation errors leads us to consider a disk with a characteristic semimajor axis of $a_* = 200$. To allow the MRI ample time to grow, the disk should not evolve too rapidly under hydrodynamics; therefore, we consider a moderate eccentricity of $e = 0.4$, a bit smaller than the $e = 0.5$ used in Chan et al. (2022). These choices imply

a characteristic semilatus rectum $\lambda_* = a_*(1 - e^2) = 168$. In the same vein, we assign to our initial disk a small sound speed, equivalent to a Mach number of ≈ 30 at pericenter.

2.2. Equations

We follow the conventions of Gammie et al. (2003). The metric signature is $(-, +, +, +)$, Greek indices range over $\{0, 1, 2, 3\}$, Latin indices range over $\{1, 2, 3\}$, and Einstein summation is implied. The equations of GRMHD are

$$\partial_t [(-g)^{1/2} \rho u^t] + \partial_j [(-g)^{1/2} \rho u^j] = 0, \quad (1)$$

$$\partial_t [(-g)^{1/2} T_\mu^t] + \partial_j [(-g)^{1/2} T_\mu^j] = (-g)^{1/2} T_\sigma^\nu \Gamma_{\mu\nu}^\sigma, \quad (2)$$

$$\partial_t [(-g)^{1/2} *F^{it}] + \partial_j [(-g)^{1/2} *F^{ij}] = 0. \quad (3)$$

Here t is the coordinate time, ρ is the comoving mass density, u^μ is the velocity, g is the determinant of the metric $g_{\mu\nu}$, and $\Gamma_{\mu\nu}^\sigma$ is the Christoffel symbol of the second kind. From the Hodge dual $*F^{\mu\nu}$ of the electromagnetic tensor $F^{\mu\nu}$ we obtain the magnetic field $B^i = *F^{i0}$ and the projected magnetic field $b^\mu = u_\nu *F^{\nu\mu}$. Lastly, the stress–energy tensor is

$$T^{\mu\nu} = \left(p + \frac{1}{2} b_\sigma b^\sigma \right) g^{\mu\nu} + \left(\rho + \frac{\gamma}{\gamma - 1} p + b_\sigma b^\sigma \right) u^\mu u^\nu - b^\mu b^\nu, \quad (4)$$

where p is the gas pressure. Our analysis makes use of the current, which is not tracked explicitly by the code but can be obtained in post-processing from the expression

$$j^\mu = \nabla_\nu F^{\mu\nu} = \nabla_\nu (\epsilon^{\mu\nu\sigma\tau} u_\sigma b_\tau), \quad (5)$$

with $\epsilon^{\mu\nu\sigma\tau}$ the contravariant Levi–Civita tensor.

2.3. Eccentric coordinate system

We employ a three-dimensional coordinate system based on conventional cylindrical coordinates, modified to conform to the gas motion in an eccentric disk. The coordinate curves in the midplane are particle orbits with the initial disk eccentricity, and the expansion and contraction of the vertical coordinate matches that of the initial disk. Using such a coordinate system has multiple benefits. It is more efficient than the standard cylindrical coordinate system because the simulation domain fits more tightly around the disk, and because there is no need to allocate cells to regions far away from the disk. Cells are shorter near pericenter where the disk is thinner and taller near apocenter where the disk is thicker, so the level to which disk mass is resolved is more azimuthally uniform. Streamlines are less oblique to the grid, reducing numerical dissipation and numerical artifacts. The initial velocity and magnetic field can also be set in a much cleaner fashion.

The eccentric coordinate system is derived from the cylindrical coordinate system in two orthogonal steps: first, by substituting cylindrical coordinate surfaces with elliptical ones that match the initial disk eccentricity; second, by deforming horizontal coordinate surfaces into oblique conical ones that approximately track disk breathing. The intersection of the elliptical coordinate surfaces with the midplane are orbits followed by material in the initial disk.

The eccentric coordinate system is parametrized by (e, λ_*) , where e is the initial disk eccentricity and λ_* is the characteristic

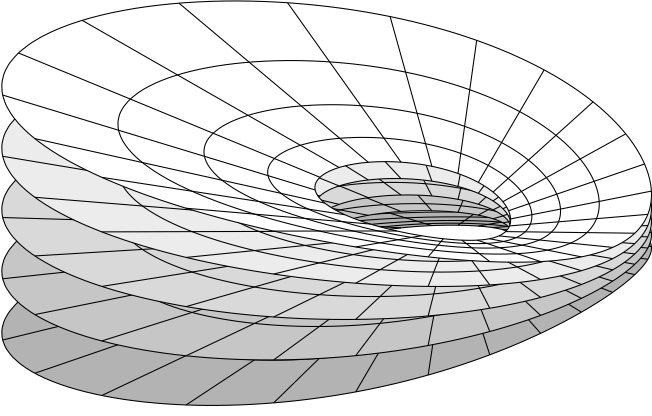


Figure 1. Coordinate surfaces of constant ζ for one instance of the eccentric coordinate system.

semilatus rectum of the orbit along which we compute the expected amplitude of disk breathing for use in constructing the grid. One instantiation of the eccentric coordinate system is illustrated in Figure 1.

More explicitly, let (t, R, φ, z) be cylindrical coordinates. We assume the weak-gravity limit, so the only nonzero components of the metric are

$$g_{tt} = -(1 + 2\Phi), \quad (6)$$

$$g_{RR} = 1, \quad (7)$$

$$g_{\varphi\varphi} = R^2, \quad (8)$$

$$g_{zz} = 1. \quad (9)$$

Chan et al. (2022) proved that closed elliptical orbits exist at all semilata recta for the quasi-Newtonian potential

$$\Phi(R, z) = -1/[R^2 + z^2]^{1/2} + 2]. \quad (10)$$

Eccentric coordinates $(t, \ln \lambda, \phi, \zeta)$ are derived from cylindrical coordinates through the coordinate transformation

$$R = \lambda/(1 + e \cos \phi), \quad (11)$$

$$\varphi = \phi, \quad (12)$$

$$z = \zeta H_*(e; \phi) \lambda / \lambda_*. \quad (13)$$

We can reuse t for the new coordinates without ambiguity because it does not enter into the coordinate transformation.

Logarithmic scaling in the semilateral rectus direction is built into the eccentric coordinate system. The rest of this article will not mention the $(\ln \lambda)$ -coordinate itself; measurements along that direction will be converted to λ first for ease of comprehension. A caveat is that whenever a component is labeled with λ , it is understood that the $(\ln \lambda)$ -coordinate is referred to. Grid breathing is controlled by the arbitrary grid height function H_* , which should reduce to a constant function when $e = 0$. The metric and connection are listed in Appendix A.

One way of fixing H_* utilizes a reference gas column that mimics the initial disk. The column obeys the same adiabatic equation of state $p \propto \rho^\gamma$ as the disk, is isentropic for simplicity, and has surface density Σ_* and entropy typical of the initial disk at the characteristic orbit $\lambda = \lambda_*$. As we shall see in Section 2.4, the surface density of our initial disk depends only on λ , so the

choice of Σ_* is straightforward. However, because our initial disk is not in general isentropic, the proportionality constant K_* in the equation of state can be only loosely related to the initial disk entropy, and Section 2.4 will explain how it is picked. The column so constructed is placed at different ϕ along the characteristic orbit, and the scale height of the column under vertical force balance is our $H_*(\phi)$. The details are relegated to Appendix B. Because the location of the column is determined by (e, λ_*, ϕ) and the gas in the column is parametrized by (γ, Σ_*, K_*) , the full dependence of H_* is $H_*(e, \lambda_*, \gamma, \Sigma_*, K_*; \phi)$.

We emphasize that the choice of H_* is arbitrary and has no physical implications. The breathing of our grid captures only part of the breathing of the actual disk: Our H_* is based on an adiabatic hydrostatic column, whereas vertical motion in an actual disk exhibits inertia, and the accumulation of dissipated energy can also puff up the disk. We could use more elaborate methods to determine H_* (e.g., Ogilvie & Barker 2014), but our approximate prescription has the advantage that H_* and its derivatives have simple expressions.

2.4. Initial condition

We would like to start our simulation with an eccentric disk as close to force balance as possible, both horizontally and vertically. To do so, we deform a circular disk that is strictly in hydrostatic equilibrium into an eccentric disk that is approximately so. The result is exhibited in the left column of Figure 2. What follows is a sketch of the deformation procedure; technicalities are left to Appendix C.

Our starting point is a circular disk. The density maximum of the disk is along $R = \lambda_*$, where $\lambda_* = 168$ is the characteristic semilatus rectum of the eccentric disk we would like to arrive at. We match the circular and eccentric disks in semilatus rectum in order that the two disks have the same characteristic specific angular momentum. The circular disk is both horizontally and vertically thin: Starting from the density maximum, the density falls by one e -folding if we move to $R \approx 0.86 \lambda_*$ or $R \approx 1.18 \lambda_*$ along the midplane, or to $|z| \approx 9$ vertically. The Mach number of the disk is ≈ 30 .

The circular disk is converted into an initial condition. The initial condition uses a realization of the eccentric coordinate system adapted to the disk, with $e = 0$ and a constant $H_*(e = 0; \phi)$ matched to disk conditions. We do not use the initial condition directly; instead, with the circular disk already set up in coordinate space, we turn it eccentric simply by changing e of the coordinate system to some finite value. This reinterpretation of the initial condition simultaneously makes $H_*(e; \phi)$ a function of ϕ . Because the density distribution of the disk follows coordinate surfaces, the poloidal cross-section of the disk expands and contracts over azimuth the same way the grid does. Furthermore, the varying cross-section implies the velocity should have a nonzero vertical component, which our procedure guarantees because the velocity stays parallel to the coordinate curves.

We paint on the eccentric disk a dipolar magnetic field derived from a magnetic potential whose only nonzero component is

$$A_\phi(\lambda, \phi, \zeta) \propto (-g)^{1/2} \max\{0, \rho - \frac{1}{2} \max_{\lambda', \zeta'} \rho(\lambda', \phi, \zeta')\}; \quad (14)$$

for intuition, $\hat{e}^\phi = \hat{e}^\varphi$ is a one-form that can be visualized as a family of poloidal planes. Including the metric determinant in the magnetic potential makes the magnetic field strength more

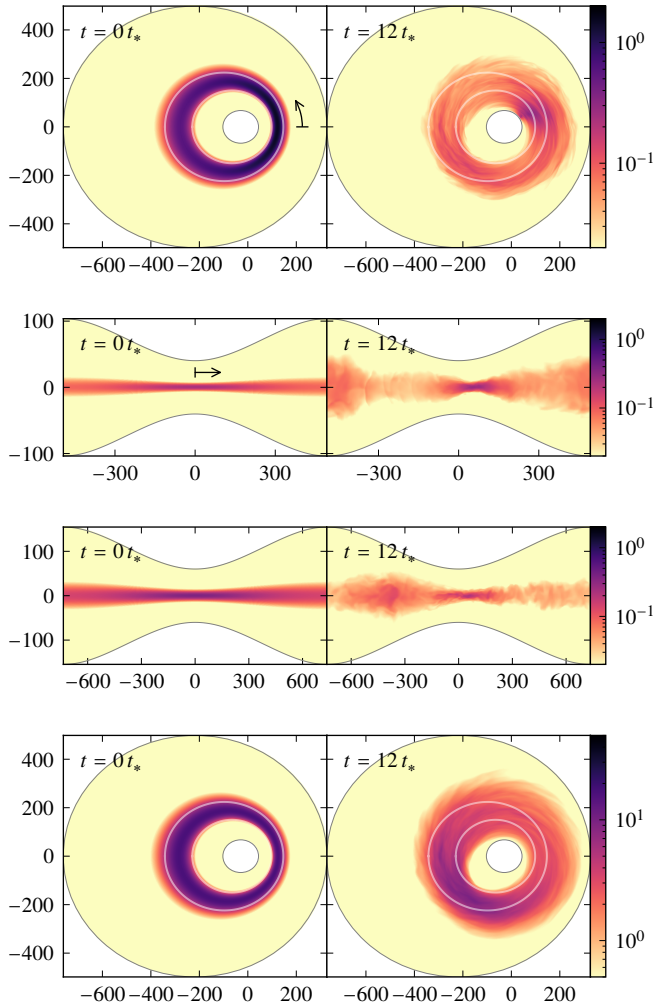


Figure 2. Density in the top three rows and surface density in the bottom row. The top row shows midplane slices of density, the middle two rows show vertical slices of density along $\ln(\lambda/\lambda_*) = \pm 0.2$, respectively, on either side of the characteristic orbit, and the bottom row shows surface density. The boundaries of the simulation domain are traced by thin gray curves. For the top and bottom rows, the ellipses along which vertical slices are taken are indicated by faint white ellipses. For the middle two rows, the abscissa is the physical arc length along the characteristic orbit measured from $\phi = 0$, the ordinate is the physical height z above the midplane, and the ordinate is more stretched than the abscissa. The two arrows in the top two rows indicate how ϕ is defined: The tick is where $\phi = 0$ and the arrow points in the direction of increasing ϕ .

uniform over azimuth, and using the maximum density in the same poloidal slice instead of the global maximum ensures all poloidal planes are magnetized. The proportionality constant is picked such that the volume-integrated plasma beta, or the ratio of volume-integrated gas pressure to volume-integrated magnetic pressure, is 100. After the magnetic field is added, we reduce the gas pressure so as to keep the total pressure the same as before, and we perturb the gas pressure at the 0.01 level to seed the MRI.

2.5. Simulation domain, boundary conditions, and other numerical concerns

The simulation domain occupies the volume $[\exp(-1)\lambda_*, \exp(1)\lambda_*] \times [-\pi, \pi] \times [-6, 6]$ in (λ, ϕ, ζ) . The vertical extent at the characteristic orbit needs to be six times the scale height of the reference column to capture the gas and magnetic field at high altitudes. The grid is linear in coordinate space in all three directions, the cell count is $640 \times 960 \times 270$, and the cell aspect ratio is $\approx 1 : 2 : 1$. The simulation formally terminates at $t = 12 t_*$, where $t_* = 2\pi a_*^{1/2} (a_* + 2)$ is the orbital period at the characteristic orbit, but we allow the simulation to run for $0.5 t_*$ more so we can perform time-averages centered around the end. This simulation duration is sufficient for the MRI to reach nonlinear saturation, but it is much too short for the parametric instability of Papaloizou (2005a,b) to appear.

The boundary conditions are outflow in the semilateral rectus direction, periodic in the azimuthal direction, and outflow in the vertical direction. To implement the outflow boundary condition, we copy all quantities to the ghost zone, zero the λ -component of the velocity wherever it points into the simulation domain, and zero the ϕ - and ζ -components of the projected magnetic field.

Lastly, when the recovery of primitive variables fails, we carry over primitive variables from the previous time step.

3. RESULTS

3.1. Summary

In terms of gas properties, the stratified disk behaves much like the unstratified eccentric disk in Chan et al. (2022) with a dipolar magnetic topology: Gas spreads both inward and outward over the course of the simulation, as we can see in Figure 2.

During this time, the stratified disk as a whole remains eccentric, but eccentricity rises at small radii and decreases at large radii as MHD stresses transport angular momentum outward. The inner parts of the disk undergo prograde apsidal precession during $t \lesssim 2 t_*$, but this precession then ceases.

An important difference between the stratified disk and our earlier unstratified one is that the stratified disk puffs up over time. In the stratified case, vertical expansion is due to the adiabatic equation of state retaining the internal energy created by dissipation of orbital energy. Figure 3 shows an increase in internal energy by a factor of ~ 4 to 5 by the end of the simulation. In the unstratified case, the isothermal equation of state prevents any such internal energy retention, and the absence of vertical gravity means vertical hydrostatic balance is irrelevant in any event.

In terms of magnetic properties, we consider the ratio α_m of Maxwell stress to pressure, which is the Shakura & Sunyaev (1973) α parameter but ignoring for simplicity the contribution from the Reynolds stress. The stratified disk resembles its unstratified counterpart in that α_m , portrayed in Figure 4, is consistently positive in one half of the disk and negative in the other half.

Figure 3 charts how the magnetic energy per mass surges to a peak value ~ 200 to 300 times the initial value during the first half of the simulation, then drops by a factor of ~ 3 to 4 during the second half. Weaker magnetization at late times is accompanied by a smaller α_m . This magnetic field decay may

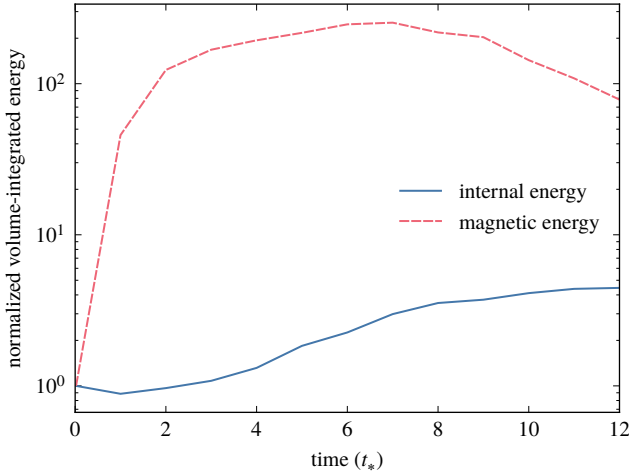


Figure 3. Volume-integrated internal and magnetic energies, divided by volume-integrated density to account for mass loss from the simulation domain. Each curve is normalized to unity at $t = 0$ to emphasize variation over time.

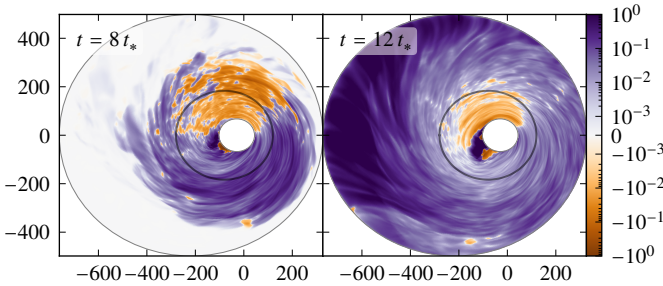


Figure 4. Mass-weighted vertical averages of the Maxwell-only alpha parameter. The boundaries of the simulation domain are traced by thin gray curves and the characteristic orbit $\lambda = \lambda_*$ is indicated by a faint black ellipse.

be partly due to reconnection driven by compression resulting from the strong vertical gravity near pericenter.

3.2. Gas behavior

3.2.1. Radial and vertical expansion

As Figure 2 makes clear, the disk expands dramatically both radially and vertically over the 12 orbits of the simulation. One way to quantify this spreading is to note that, at $t = 0$, $\approx 86\%$ of the mass is contained within $|\ln(\lambda/\lambda_*)| \leq 0.2$, or $138 \leq \lambda \leq 205$, whereas the same fraction of the mass at $t = 12 t_*$ is found within $|\ln(\lambda/\lambda_*)| \leq 0.53$, or $99 \leq \lambda \leq 285$. In other words, the disk is roughly two to three times wider both inward and outward.

The vertical expansion seen in the middle rows of Figure 2 is the product of internal energy accumulation: Figure 3 demonstrates that the ratio of volume-integrated gas pressure to volume-integrated density of the stratified disk rises steadily at $t \gtrsim 3 t_*$, albeit at slower rates toward the end. For the unstratified disk with a dipolar magnetic topology, the same diagnostic scarcely changes at all, as expected from the use of an isothermal equation of state.

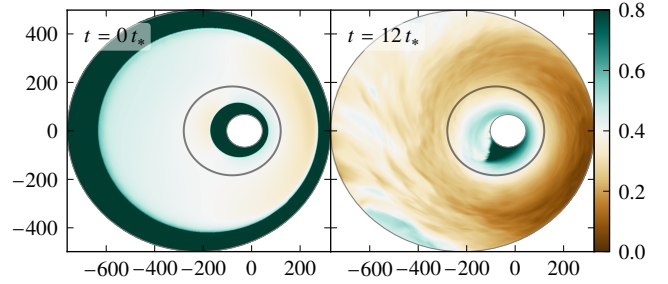


Figure 5. Mass-weighted vertical averages of the instantaneous eccentricity. The boundaries of the simulation domain are traced by thin gray curves and the characteristic orbit $\lambda = \lambda_*$ is indicated by a faint black ellipse.

3.2.2. Eccentricity and orientation

To quantify eccentricity evolution, we compute the instantaneous eccentricity \bar{e} , which is the eccentricity of the orbit a gas packet would follow given its velocity if there were no forces other than gravitational. We use a definition similar to Chan et al. (2022), but to account for the effect of vertical gravity, we first project the velocity to the midplane before calculating \bar{e} ; Appendix D describes how this is done. Figure 5 depicts the mass-weighted vertical average of the instantaneous eccentricity:

$$\langle \bar{e} \rangle_{\zeta, \rho} \equiv \int d\zeta (-g)^{1/2} \rho \bar{e} \Big/ \int d\zeta (-g)^{1/2} \rho. \quad (15)$$

Henceforth when mentioning averages like this, we drop for brevity the subscript detailing how the average is performed. At the start of the simulation, $\langle \bar{e} \rangle \approx 0.4$ over the entire disk. Small deviations indicate non-Keplerian rotation, present because the circular disk on which the initial eccentric disk is based features non-Keplerian rotation due to pressure gradients. At the end of the simulation, $0.3 \lesssim \langle \bar{e} \rangle \lesssim 0.4$ near the characteristic orbit, $0.3 \lesssim \langle \bar{e} \rangle \lesssim 0.5$ inside it, and $0.2 \lesssim \langle \bar{e} \rangle \lesssim 0.4$ outside. The most extreme $\langle \bar{e} \rangle$ is found in regions farthest away from the characteristic orbit, both inside and outside, but the great majority of these regions have very low density according to Figure 2.

Figure 6 depicts the mass distribution over specific binding energy $E_b = 1 - E$ and specific angular momentum L , where E is the specific energy inclusive of rest energy. At all times, $\ln L$ is linearly correlated with $\ln E_b$ to a good approximation. MHD stresses increase the gradient of this correlation by transferring L from the inner parts of the disk with lower initial L to the outer parts with higher initial L . Compared to the large fractional change in L^2 , the fractional change in E_b is much smaller; the net result is that the slope of the correlation steepens from an initial value of $-\frac{1}{2}$ to ~ -0.6 at $t = 12 t_*$ with a slightly steeper slope for low- L material. Because $E_b L^2 \approx \frac{1}{2}(1 - \bar{e}^2)$ if $E_b \ll 1$, eccentricity rises in the inner parts and falls in the outer parts.

Another view of the eccentricity evolution is provided by Figure 7, which compares the mass distribution over \bar{e} of the stratified disk with two unstratified disks from Chan et al. (2022). All three disks have narrow initial distributions that spread over time; the spread is very slow for the unstratified unmagnetized disk and fastest for the stratified disk. The unstratified distributions acquire a bimodal shape centered on the initial \bar{e} , whereas the stratified distribution remains unimodal and shifts toward smaller \bar{e} . The apparent asymmetry of the stratified distribution

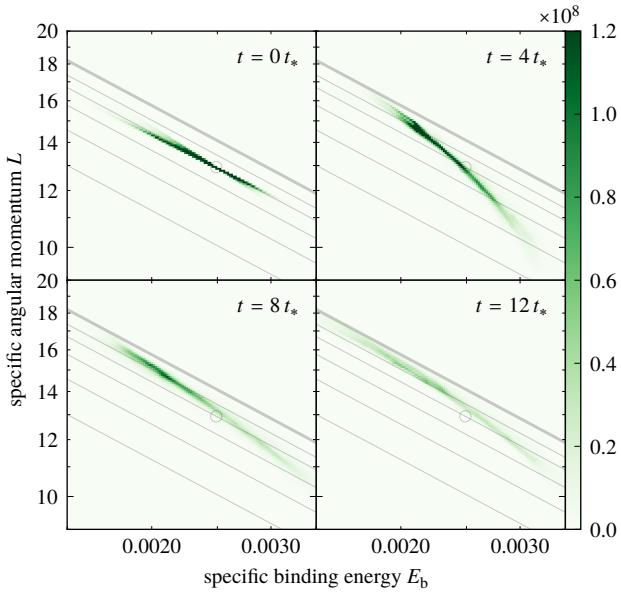


Figure 6. Mass-weighted two-dimensional histograms of specific binding energy E_b and specific angular momentum L . The histograms are normalized by the initial mass and the axes are logarithmic. The small faint circle marks the E_b and L of the characteristic orbit $\lambda = \lambda_*$. The faint lines trace, in order from top to bottom, the combinations of E_b and L for which $\bar{e} \in \{0, 0.3, 0.4, 0.5, 0.6, 0.7\}$; the histograms are practically zero above the thick $\bar{e} = 0$ line.

is partly because material with $0.60 \lesssim \bar{e} \lesssim 0.75$ has such small pericentric distances that it is lost through the inner boundary; $\sim 9\%$ of the initial mass is lost thusly.

The extent to which the stratified disk undergoes apsidal precession can be determined by tracking the azimuth of the pericenter, which is also the thinnest part of the disk. Figure 2 shows the inner parts of the disk undergo reorientation: They precess by $\sim \frac{1}{6}\pi$ in the prograde direction within $t \lesssim 2 t_*$ and stay at roughly that orientation for the rest of the simulation. In comparison, the outer parts do not alter their orientation appreciably. Similar to the unstratified disks in Chan et al. (2022), apsidal precession in the stratified disk is limited both in duration and extent; hence, its long-term effect is likely small.

The transient apsidal precession in our stratified and unstratified simulations reflects the relaxation of the disk from its initial condition. It should be distinguished from the secular pressure-induced apsidal precession discussed in other contexts of eccentric disks (e.g., Statler 2001). The rate of such apsidal precession is of order the orbital frequency divided by the square of the Mach number (Murray & Dermott 1999), which is much slower than the apsidal precession we witness.

3.2.3. Disk height

The initial disk breathing matches grid breathing perfectly by construction, but the disk gradually drifts away from that perfect match over time. Apart from apsidal precession, we can see other signs of mismatch by the end of the simulation in the middle rows of Figure 2: The disk height near apocenter rises by a factor of ~ 2.5 over the course of the simulation but hardly changes near pericenter, and the density distribution and disk height are no longer symmetric about the line of apsides. The larger apocenter-to-pericenter disk height ratio than grid height

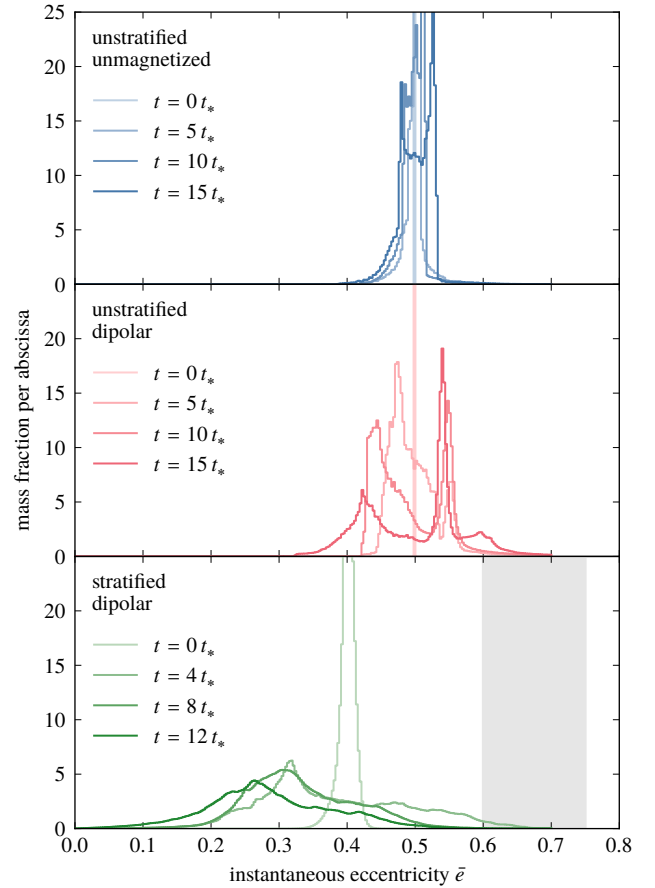


Figure 7. Mass-weighted histograms of instantaneous eccentricity for several eccentric disks. The top and middle panels are for two unstratified disks from Chan et al. (2022), the top panel for the unmagnetized disk and the middle panel for the disk with a dipolar magnetic topology. The bottom panel is for the stratified disk from this article, which also has a dipolar magnetic topology; the gray band approximately indicates the \bar{e} of the material crossing the inner boundary.

ratio was anticipated in Section 2.3.

For a more quantitative examination of the disk height modulation, we calculate the mass-weighted distance from the midplane:

$$\langle |z| \rangle_{t, \lambda, \zeta, \rho} \equiv \int dt d \ln \lambda d \zeta (-g)^{1/2} \rho |z| \int dt d \ln \lambda d \zeta (-g)^{1/2} \rho. \quad (16)$$

The temporal integration limits are $11.5 t_* \leq t \leq 12.5 t_*$; time-averaging is done in consistency with the magnetic quantities discussed in Section 3.3, which require time-averaging to smooth out strong spatial fluctuations. The spatial integration limits are $-0.2 \leq \ln(\lambda/\lambda_*) \leq 0.2$ and all ζ ; although the disk evolves in eccentricity and orientation, we stick to an elliptical annulus around the characteristic orbit for simplicity. The top panel of Figure 8 traces $\langle |z| \rangle$, or rather its reciprocal, in anticipation of how other quantities in the same figure behave. We also show the reciprocal H_*^{-1} of the grid height for context. The modulation of $\langle |z| \rangle$ around the orbit is stronger than H_* . The extrema of $\langle |z| \rangle$ are displaced in azimuth by $\sim \frac{1}{6}\pi$ from those of H_* , reflecting apsidal precession.

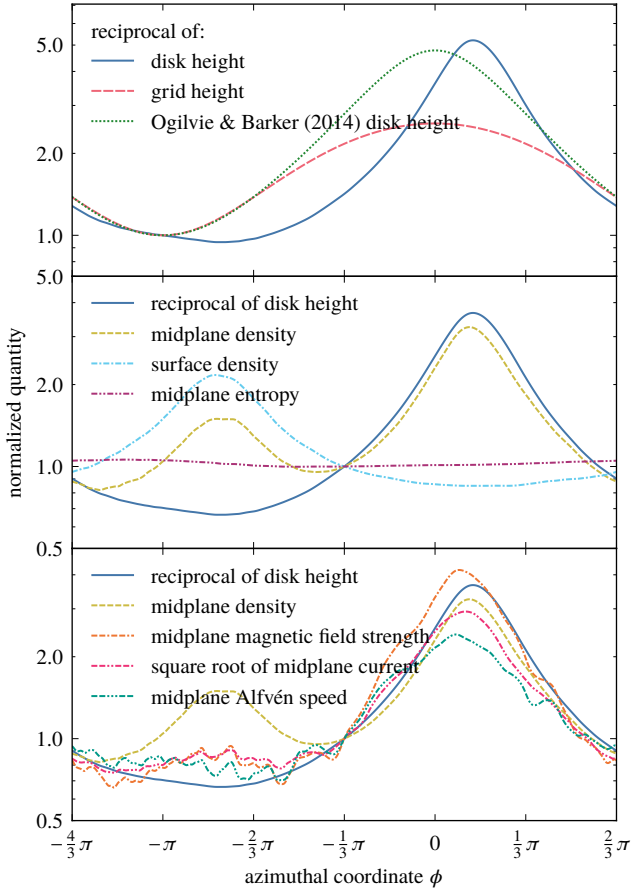


Figure 8. Azimuthal modulation along the characteristic orbit $\lambda = \lambda_*$ at $t = 12 t_*$; see Sections 3.2 and 3.3 for definitions. The abscissa is shifted so that the apocentric region fits in the left half of each panel and the pericentric region in the right half. To emphasize relative change, the curves in the top, middle, and bottom panels are normalized by their values at the arbitrarily chosen azimuths $\phi = -\pi$, $\phi = -\frac{1}{3}\pi$, $\phi = -\frac{1}{3}\pi$, respectively.

Ogilvie & Barker (2014) wrote down the equation governing the height of a laminar eccentric disk that expands and contracts homologously in the vertical direction. We reproduce in the same panel the reciprocal of the solution to their equation for a uniformly eccentric disk with the same eccentricity and adiabatic index as our initial disk. The analytic disk height varies with an amplitude close to our $\langle |z| \rangle$, but the rise and fall of our $\langle |z| \rangle$ near pericenter is more rapid.

3.2.4. Azimuthal modulation

Next we inspect the azimuthal modulation of various hydrodynamic quantities, beginning with density ρ and surface density

$$\Sigma \equiv R^{-2} \int d\zeta (-g)^{1/2} \rho \quad (17)$$

as shown in Figure 2. The initial surface density is uniform over azimuth, hence the initial density peaks at the pericenter $\phi = 0$. Apsidal precession moves the pericenter and the density peak to $\phi \sim \frac{1}{6}\pi$; at the same time, the surface density develops a maximum at $\phi \sim -\frac{5}{6}\pi$ near apocenter.

To put this on a more quantitative footing, we construct the

azimuthal profiles of midplane density

$$\langle \rho \rangle_{t,\lambda,\zeta} \equiv \int dt d \ln \lambda d\zeta (-g)^{1/2} \rho \bigg| \int dt d \ln \lambda d\zeta (-g)^{1/2} \quad (18)$$

and surface density

$$\langle \Sigma \rangle_{t,\lambda} \equiv \int dt d \ln \lambda d\zeta (-g)^{1/2} \rho \bigg| \int dt d \ln \lambda R^2. \quad (19)$$

The integration limits for $\langle \Sigma \rangle$ are the same as for $\langle |z| \rangle$ in Equation (16), and those for $\langle \rho \rangle$ differ only in that $-0.2 \leq \zeta \leq 0.2$, to pick out the midplane. The results are displayed in the middle panel of Figure 8, along with the reciprocal $\langle |z| \rangle^{-1}$ of the disk height. The secondary peak of $\langle \rho \rangle$ at $\phi \sim -\frac{5}{6}\pi$ is barely noticeable in Figure 2. Over $-\frac{1}{3}\pi \leq \phi \leq \frac{2}{3}\pi$ around pericenter, we have $\langle \rho \rangle \propto \langle |z| \rangle^{-1}$ and constant $\langle \Sigma \rangle$, consistent with pure vertical compression; over $-\frac{4}{3}\pi \leq \phi \leq -\frac{1}{3}\pi$ around apocenter, we still have $\langle \rho \rangle \propto \langle |z| \rangle^{-1}$, but the non-constancy of $\langle \Sigma \rangle$ implies that, unlike in the initial disk, horizontal motion is not divergence-free.

Following up on the increase in internal energy due to dissipation shown in Figure 3, we graph in the same panel of Figure 8 a proxy for the mass-weighted midplane entropy,

$$\langle s \rangle_{t,\lambda,\zeta;\rho} \equiv \int dt d \ln \lambda d\zeta (-g)^{1/2} \rho \ln(\rho/\rho^\gamma) \bigg| \int dt d \ln \lambda d\zeta (-g)^{1/2} \rho, \quad (20)$$

reusing here the integration limits for $\langle \rho \rangle$ in Equation (18). The flatness of $\langle s \rangle$ indicates that, in this simulation with heating but no cooling, entropy growth is slow compared to orbital motion by the end of the simulation.

3.3. Magnetic behavior

3.3.1. Magnetic field strength and Maxwell stress

The magnetic field grows in a way similar to circular disks. The initial magnetic field is symmetric about the midplane. As the simulation progresses, differential rotation draws out magnetic fields, the MRI grows in amplitude from small to nonlinear, parasitic instabilities break up the smooth azimuthal variation of the magnetic field (e.g., Goodman & Xu 1994), and full three-dimensional turbulence begins to grow. The symmetry about the midplane lasts until $t \sim 6 t_*$, shortly after the ordered stage of magnetic field growth ends, but shortly before the volume-integrated magnetic energy reaches a maximum at $t \sim 7 t_*$, according to Figure 3. Thereafter, the magnetic field becomes increasingly turbulent even while the volume-integrated magnetic energy decays.

The bottom panel of Figure 8 traces the azimuthal profile of the midplane magnetic field strength

$$\langle b \rangle_{t,\lambda,\zeta} \equiv \left[\int dt d \ln \lambda d\zeta (-g)^{1/2} b_\mu b^\mu \bigg| \int dt d \ln \lambda d\zeta (-g)^{1/2} \right]^{1/2}. \quad (21)$$

The integration limits are the same as $\langle \rho \rangle$ in Equation (18). Over $-\frac{1}{3}\pi \leq \phi \leq \frac{2}{3}\pi$ around pericenter, vertical compression and flux

freezing explains why $\langle b \rangle \propto \langle |z| \rangle^{-1}$. The symmetric rise and fall of $\langle b \rangle$ during pericenter passage suggests that the magnetic field is not noticeably amplified by effects other than compression. This nonlinear-stage behavior is different from the pericentric amplification seen in linear-stage MRI (Chan et al. 2018).

To compute the Maxwell stress in cylindrical coordinates, we need the physical, cylindrical components $b^{\hat{i}}$ of the projected magnetic field, that is, the components measured in a local orthonormal basis whose basis vectors are parallel to those of cylindrical coordinates. They are related to the contravariant components b^i by

$$b^{\hat{R}} = R \left(b^\lambda + b^\phi \frac{e \sin \phi}{1 + e \cos \phi} \right), \quad (22)$$

$$b^{\hat{\phi}} = R b^\phi, \quad (23)$$

$$b^{\hat{z}} = z \left(b^\lambda + b^\phi \frac{d}{d\phi} \ln H_* + \frac{b^\zeta}{\zeta} \right), \quad (24)$$

and they satisfy the normalization

$$g_{ij} b^i b^j = b^{\hat{R}} b^{\hat{R}} + b^{\hat{\phi}} b^{\hat{\phi}} + b^{\hat{z}} b^{\hat{z}}. \quad (25)$$

Following Chan et al. (2022), we ignore the contribution of the Reynolds stress to the total internal stress on the assumption that the Maxwell stress dominates, an extrapolation from circular disks (e.g., Hawley et al. 1995). The Maxwell-only alpha parameter is

$$\alpha_m = -b^{\hat{\phi}} b^{\hat{R}} / p. \quad (26)$$

Figure 4 depicts the vertical averages of α_m at $t = 8 t_*$ and $t = 12 t_*$:

$$\langle \alpha_m \rangle_{\zeta;p} \equiv - \int d\zeta (-g)^{1/2} b^{\hat{\phi}} b^{\hat{R}} \Big/ \int d\zeta (-g)^{1/2} p. \quad (27)$$

The magnitude of $\langle \alpha_m \rangle$ at both times is $10^{-3} \lesssim |\langle \alpha_m \rangle| \lesssim 10^{-1}$, roughly comparable to the values seen in global simulations of circular disks (e.g., Hawley 2000; Hawley & Krolik 2002). However, the negative sign of $\langle \alpha_m \rangle$ in the half of the disk where material flows outward from pericenter to apocenter is never seen in circular disks, but is found in unstratified eccentric disks (Chan et al. 2022). We therefore identify this sign flip with the same mechanism responsible for it in the unstratified case, that is, the change in sign of $\partial u^{\hat{R}} / \partial \phi$, which alters the correlation of $b^{\hat{R}}$ and $b^{\hat{\phi}}$ created by orbital shear. Consistent with this interpretation, at $t = 8 t_*$ the $\langle \alpha_m \rangle < 0$ region stretches across the entire radial extent of the disk, whereas at $t = 12 t_*$ when the outer parts of the disk are substantially less eccentric, the $\langle \alpha_m \rangle < 0$ region is more limited in size.

The same figure shows that the magnitude of $\langle \alpha_m \rangle$ declines over time: $3 \times 10^{-3} \lesssim |\langle \alpha_m \rangle| \lesssim 3 \times 10^{-1}$ at $t = 8 t_*$ but $10^{-3} \lesssim |\langle \alpha_m \rangle| \lesssim 10^{-1}$ at $t = 12 t_*$. We associate the late-time decline with a general weakening of the magnetic field after $t \gtrsim 7 t_*$, as illustrated in Figure 3. This effect may be attributable to the strong reconnection in stratified eccentric disks, an idea we explore further in Section 3.3.2.

Another way to average α_m is over constant- R cylinders, taking into account the 10 to 20% contribution of $\alpha_m < 0$ regions to the average. On cylinders running through denser parts of the disk, this average rises rapidly to ~ 0.1 at $t \sim 2 t_*$, falls to ~ 0.05

at $t \sim 5 t_*$ as the MRI turns nonlinear, and dwindles to ~ 0.01 at $t \sim 12 t_*$ with the gradual diminution of the magnetic field. At $t \gtrsim 8 t_*$, α_m is inversely correlated with \bar{e} : α_m averaged on cylinders at $R \sim 300$, where orbits are less eccentric, is a few times that on cylinders at $R \sim 200$.

3.3.2. Reconnection

Reconnection is the principal mechanism for magnetic field decay. Because MHD simulations do not resolve the microscopic scales on which physical reconnection occurs, reconnection in a simulation like ours is necessarily numerical: Oppositely directed magnetic fields advected into the same cell cancel each other. Reconnection in our simulation happens in regions of strong magnetic shear, a measure of which is $\nabla_\nu F^{\mu\nu} = j^\mu$; its magnitude $(j_\mu j^\mu)^{1/2}$ is the magnitude of the usual three-current in the comoving frame. Studies of magnetic dissipation in grid-based simulations have found that the dissipation rate scales with the current magnitude slightly faster than linearly (Hirose et al. 2006).

It is therefore instructive to plot $(j_\mu j^\mu)^{1/2}$, as in Figure 9. The current is strongly enhanced near pericenter because pericentric compression both strengthens the magnetic field and sharpens its gradient. To examine its azimuthal variation more quantitatively, we consider the midplane current magnitude

$$\langle j \rangle_{t,\lambda,\zeta} \equiv \left[\int dt d \ln \lambda d\zeta (-g)^{1/2} j_\mu j^\mu \Big/ \int dt d \ln \lambda d\zeta (-g)^{1/2} \right]^{1/2}, \quad (28)$$

the integration limits being the same as $\langle \rho \rangle$ in Equation (18). The bottom panel of Figure 8 shows that $\langle j \rangle \propto \langle |z| \rangle^{-2}$. This scaling results from the magnetic field strength growing as $\propto \langle |z| \rangle^{-1}$ when toroidal magnetic field is compressed vertically and the length scale of the vertical gradient varying as $\propto \langle |z| \rangle$; the current is proportional to the ratio of these two quantities.

3.3.3. Quality factors

The degree to which the MRI is resolved is assessed by quality factors. The forms adopted here are simple generalizations from Hawley et al. (2011) and are almost identical to Chan et al. (2022):

$$Q_z \equiv \frac{|b^{\hat{z}}| T}{\rho^{1/2} g_{\zeta\zeta}^{1/2} \Delta\zeta}, \quad (29)$$

$$Q_\phi \equiv \frac{|b^{\hat{\phi}}| T}{\rho^{1/2} R \Delta\phi}. \quad (30)$$

Figure 10 visualizes the quality factors at $t = 6 t_*$, when the magnetic field is strongest, and at $t = 12 t_*$, at the end of the simulation. Mass-weighted vertical averages appear in the top row:

$$\langle Q_z \rangle_{\zeta;p} \equiv \int d\zeta (-g)^{1/2} \rho Q_z \Big/ \int d\zeta (-g)^{1/2} \rho, \quad (31)$$

$$\langle Q_\phi \rangle_{\zeta;p} \equiv \int d\zeta (-g)^{1/2} \rho Q_\phi \Big/ \int d\zeta (-g)^{1/2} \rho; \quad (32)$$

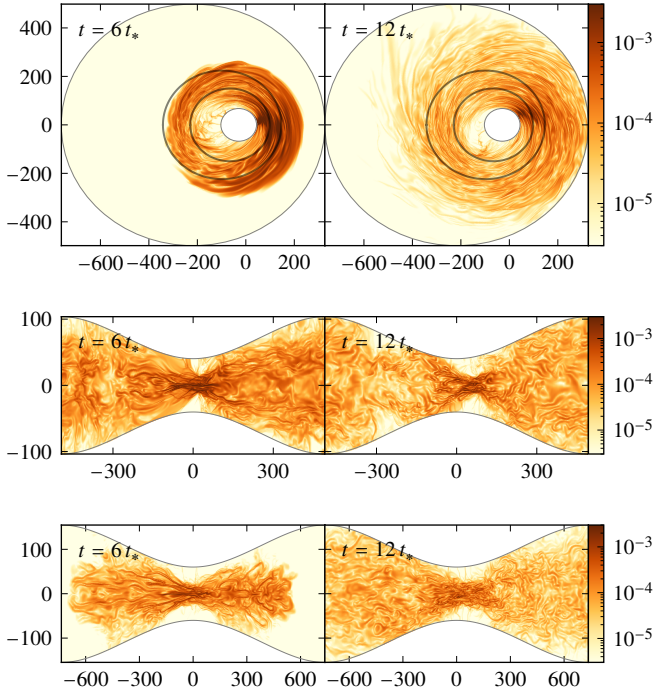


Figure 9. Magnitude of the current. The top row shows midplane slices, and the middle and bottom rows show vertical slices along $\ln(\lambda/\lambda_*) = \mp 0.2$, respectively, on either side of the characteristic orbit. The boundaries of the simulation domain are traced by thin gray curves. For the top row, the ellipses along which vertical slices are taken are indicated by faint black ellipses. For the middle and bottom rows, the abscissa is the physical arc length along the characteristic orbit measured from $\phi = 0$, the ordinate is the physical height z above the midplane, and the ordinate is more stretched than the abscissa.

raw Q_z and Q_ϕ on elliptical slices appear in the middle and bottom rows. The color scales are centered on $Q_z \gtrsim 15$ and $Q_\phi \gtrsim 20$, reflecting the criteria for adequate resolution in circular disks (Hawley et al. 2013).

There is clear azimuthal dependence of Q_z and Q_ϕ , with both being much higher near pericenter. There is also clear vertical dependence of Q_z and Q_ϕ , with both being lower near the midplane where the gas is denser and the magnetic field weaker. The former dependence can be understood by examining the azimuthal variations of v_A , H_* , and R along an orbit. The bottom panel of Figure 8 tells us that the mass-weighted midplane Alfvén speed

$$\langle v_A \rangle_{t,\lambda,\zeta;\rho} \equiv \int dt d \ln \lambda d \zeta (-g)^{1/2} \rho (b_\mu b^\mu / \rho)^{1/2} \left| \int dt d \ln \lambda d \zeta (-g)^{1/2} \rho, \quad (33) \right.$$

where the integration limits are the same as $\langle \rho \rangle$ in Equation (18), is a factor of ~ 3 higher near pericenter than near apocenter; the fact that $\langle v_A \rangle$ reaches a maximum at pericenter is consistent with our earlier observations that $\langle \rho \rangle \propto \langle |z| \rangle^{-1}$ and $\langle b \rangle \propto \langle |z| \rangle^{-1}$. We can see from the top panel of the same figure that H_* is a factor of ≈ 2.6 lower near pericenter, and we can also convince ourselves using elementary geometry that R is a factor of $(1+e)/(1-e) \approx 2.3$ lower. It follows that both $Q_z \propto v_A/H_*$ and $Q_\phi \propto v_A/R$ are maximum near pericenter, meaning that the MRI is best resolved there. This is in marked contrast to

hydrodynamics, which is harder to resolve near pericenter where the disk is thinnest.

The quality factors are much better at $t = 6t_*$ than $t = 12t_*$. Our extremely high resolution is able to provide at $t = 6t_*$ tolerable quality factors according to standards based on the circular MRI (Hawley et al. 2013). The situation changes by $t = 12t_*$, when the quality factors have dropped by factors of ~ 2 to 3. Unfortunately, an order-unity change in resolution quality can have strong effects on simulation quality (Hawley et al. 2013).

The question arises whether the factor of ~ 3 decline in magnetic energy per mass in Figure 3 is physical or numerical; that is, how much of it is due to strong magnetic dissipation near pericenter and how much is due to poor resolution suppressing the MRI. A weaker magnetic field, no matter the cause, demands smaller cells to resolve both the linear and nonlinear stages of the MRI, and such deterioration in resolution may precipitate further magnetic field decay. Because our resolution more than suffices to follow MRI-driven turbulence at $t = 6t_*$, we believe at least the initial decline is physical. However, the subsequent factor of ~ 3 decrease in magnetic energy per mass means the quality factors $\propto (B^2/\rho)^{1/2}$ at late times are, by definition, worse by factors of unity. The poorer resolution slows down perturbation growth and speeds up grid-scale dissipation, leading to magnetic field decay. The reduction in magnetic field strength in this stage thus has both physical and numerical aspects.

It is equally possible that the eccentric MRI may put somewhat higher demands on resolution because eccentric disks support linear MRI growth in modes with shorter wavelengths than would be possible in circular disks characterized by the same product of Alfvén speed and orbital period (Chan et al. 2018).

4. DISCUSSION

4.1. MRI and MHD stresses in eccentric disks

This is the third in a series of articles investigating whether the MRI, which has been studied extensively in circular disks, remains an instability when orbits are eccentric, and if it does, to what degree its nonlinear, saturated state resembles that found when orbits are circular. In our first article (Chan et al. 2018), we verified that the MRI remains linearly unstable in unstratified eccentric disks; its growth rate differs only by factors of unity from the circular case, but with increasing eccentricity, the range of unstable vertical wavenumbers extends well beyond the maximum in circular disks. In our second article (Chan et al. 2022), we showed that unstratified circular and eccentric disks have comparable ratios of Maxwell stress to pressure: $\langle \alpha_m \rangle \sim 10^{-2}$ when averaged on cylinders.

In this third article, we present the first calculation of the nonlinear evolution of the MRI in an eccentric disk with vertical gravity. Section 3.3.1 showcases the similarity between unstratified and stratified eccentric disks: Vertically averaged α_m has positive and negative regions, and cylindrically averaged α_m reaches ~ 0.1 within a few orbits. However, in the presence of vertical gravity, cylindrically averaged α_m eventually decays to ~ 0.01 by the end of the simulation; Section 3.3.3 discusses to what degree this diminution is physical or numerical. Nonetheless, our fully three-dimensional simulation, incorporating vertical gravity, confirms that the MRI is an inescapable

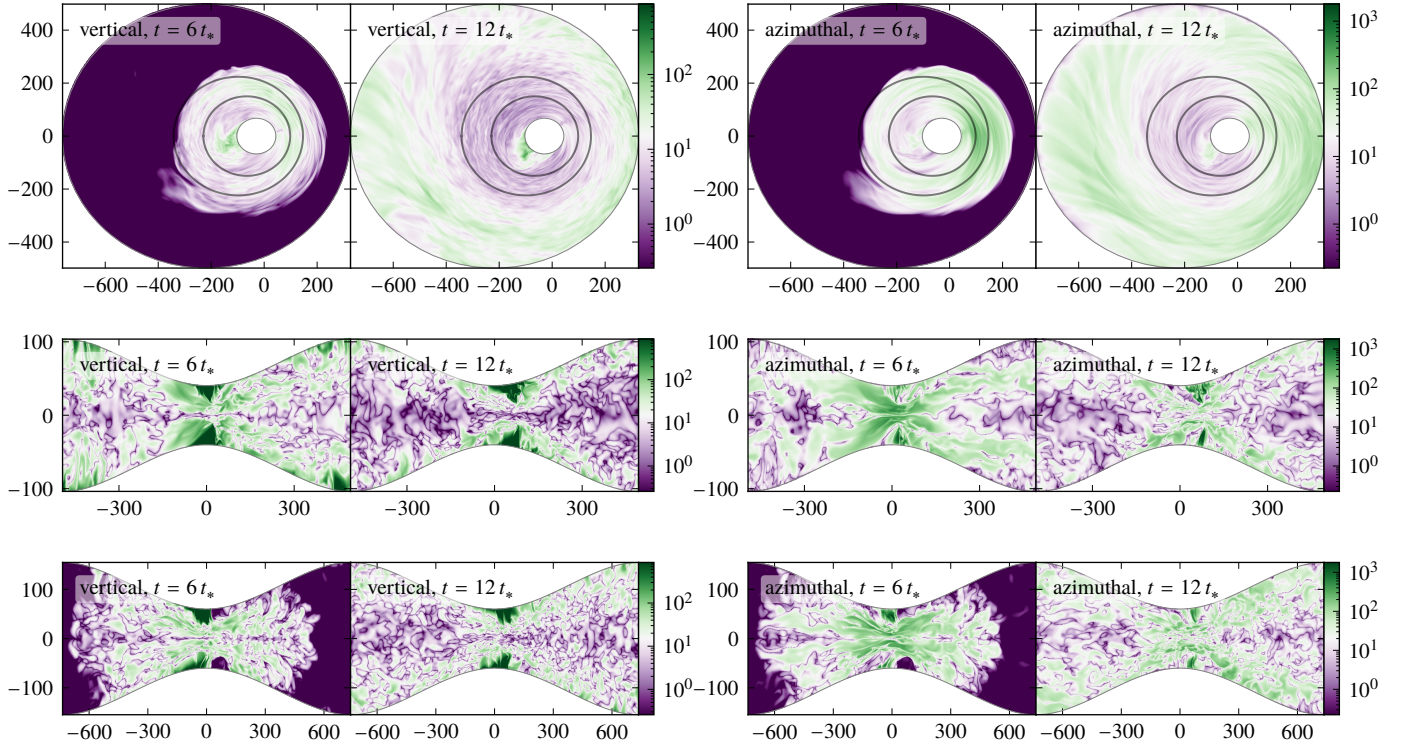


Figure 10. Vertical and azimuthal quality factors. The top row shows mass-weighted vertical averages, and the middle and bottom rows show vertical slices along $\ln(\lambda/\lambda_*) = \pm 0.2$, respectively, on either side of the characteristic orbit. The boundaries of the simulation domain are traced by thin gray curves. For the top row, the ellipses along which vertical slices are taken are indicated by faint black ellipses. For the middle and bottom rows, the abscissa is the physical arc length along the characteristic orbit measured from $\phi = 0$, the ordinate is the physical height z above the midplane, and the ordinate is more stretched than the abscissa.

feature of eccentric disks, just as it is for circular disks.

4.2. Enhanced reconnection due to vertical compression

MHD turbulence in circular disks leads to dissipation, much of which is likely due to reconnection facilitated by the mechanism suggested by Lazarian & Vishniac (1999). Our simulation uncovers a new channel specific to eccentric disks that supplements and perhaps expedites turbulent dissipation (see also the discussion by Lynch & Ogilvie 2021b).

Circular disks feature no regions of coherent compression around the orbit. By contrast, both unstratified and stratified eccentric disks can experience horizontal compression near pericenter thanks to the eccentric nature of the orbits. On top of that, stratified eccentric disks can undergo vertical compression because of the strong vertical gravity near pericenter. Vertical gravity strengthens rapidly with decreasing distance from the central object, becoming $[(1+e)/(1-e)]^3$ times stronger at pericenter than at apocenter; therefore, vertical compression can be stronger than horizontal even at moderate eccentricities. When the relative compression speed between neighboring gas packets is supersonic, shocks form that dissipate kinetic energy (Ryu et al. 2021).

In magnetized eccentric disks, horizontal and vertical compression may lead to additional dissipation as a result of reconnection. This dissipation can occur whether the compression speed is subsonic or supersonic; all it requires is that compression brings oppositely directed magnetic fields closer.

Our disk, with a dipolar magnetic topology, illustrates a condition particularly conducive to reconnection driven by vertical compression. The initial magnetic field, which is approximately radial, points in opposite directions on either side of the midplane. From this radial magnetic field, orbital shear creates azimuthal magnetic field with the same direction contrast. Converging vertical flows then produce regions of consistently powerful currents near the midplane in the pericenter region, visible in Figures 8 and 9; these regions of strong current are sites of intense magnetic dissipation in our simulation. We speculate that the additional dissipation due to this compression-driven reconnection causes the magnetic energy in our simulation to decline after reaching a maximum at $t \sim 7t_*$. We further speculate that at $t \geq 8t_*$, the reduction in eccentricity and compression-driven dissipation at large radii leads to the increase in cylindrically averaged α_m with R noted in Section 3.3.1.

Our argument for a boost in reconnection due to vertical compression rests on the horizontal magnetic field reversing direction across the midplane. In addition to our dipolar magnetic topology, this could also occur with a toroidal magnetic field if adjacent field loops point in opposite directions. Other magnetic topologies may not share this property. A toroidal magnetic field may avoid accelerated reconnection if all of its field loops point in a single direction. Likewise, a quadrupolar magnetic field with two poloidal field loops above and below the midplane may not suffer elevated levels of dissipation because the region of greatest compression around the midplane has magnetic field running in the same direction.

4.3. Rapidity of MHD-driven evolution in eccentric disks

Global MHD simulations of circular disks generally exhibit an initial transient stage of structural change on the orbital timescale, followed by an extended period of gradual evolution on the inflow timescale. Two-dimensional, purely hydrodynamical investigations of uniformly eccentric disks show that pressure forces can reshape the disk on the secular timescale (e.g., Murray & Dermott 1999), but the disk can retain its eccentricity and orientation distributions, precessing rigidly, if it starts in an eccentric mode (e.g., Statler 2001).

In sharp contrast to these outcomes, Section 3.2.2 demonstrates that MHD stresses in an eccentric disk can transform the radial profile of eccentricity \bar{e} and alter disk structure over just ~ 5 to 10 orbits. This may be surprising at first glance given that α_m indicates MHD stresses comparable to the ones driving much slower evolution in circular disks. The key is to note that material in Figure 6 largely maintains its specific binding energy E_b throughout the simulation, and that the transfer of specific angular momentum L necessary to bring about a change in \bar{e}^2 at constant E_b depends on \bar{e} as $\partial\bar{e}^2/\partial L \propto -(1 - \bar{e}^2)^{1/2} E_b^{1/2}$. In moderately eccentric disks, a modest amount of L transfer can significantly decrease \bar{e} in parts where \bar{e} is already small, as shown in Figure 6 and the bottom panel of Figure 7.

More generally, brisk MRI growth and its concomitant rearrangement of the eccentricity distribution mean that MRI-driven MHD turbulence, not hydrodynamics, dictates the evolutionary path followed by magnetized eccentric disks.

4.4. Transience of magnetized eccentric disks

MHD-driven evolution broadens mass distribution over angular momentum, moving material with the least angular momentum closer to the central object and the material with the most angular momentum farther away. It steepens the negative correlation between specific angular momentum and specific binding energy in Figure 6 beyond the constant-eccentricity relation, making the disk in Figure 5 most eccentric on its inside and most circular on its outside. During our relatively brief simulation duration of 12 orbits, there is no indication of either trend slowing down, as Figure 6 and the bottom panel of Figure 7 make apparent, or the disk approaching anything resembling a steady state.

This continuing evolution raises the question of whether any steady-state structure exists for magnetized eccentric disks. Disk evolution is driven by outward angular momentum transport by MHD stresses, and these stresses arise from orbital shear correlating the radial and azimuthal components of the turbulent velocity and magnetic field, which is an extremely general mechanism in differentially rotating disks. Consequently, it seems unlikely that disks with properties different from ours would behave in qualitatively different ways over the timescale we examined.

A heuristic argument, closely related to the fundamental mechanism of the MRI, explains how hard it is to avoid this conclusion. If two gas packets exchange angular momentum with little change in energy, the pericenter of the gas packet losing angular momentum shrinks toward the central mass, the reverse is true for the gas packet gaining angular momentum. Mean MHD stresses always carry angular momentum outward; therefore, the gas packet that is originally closer to the central mass acquires a smaller pericentric distance, and the specific

angular momentum disparity between the gas packets widens. As this gas packet moves inward, flux-freezing suggests that the Maxwell stress per unit mass either remains the same or grows, so the characteristic timescale for angular momentum loss should stay constant or even shorten.

The end result of this process is a disk whose eccentricity declines outward, but contains progressively less and less highly eccentric material as the material accretes onto the central object; such an effect is manifest in Figure 7. Gradual circularization spells the end of a magnetized eccentric disk.

This argument strictly applies to our simulated case of an isolated disk and may be altered in the presence of external influences. Mass resupply bringing in material with different energy and angular momentum could interfere with eccentricity sorting. Gravitational perturbations from another object could modify the energy and angular momentum budget of the disk. However, because MHD-driven evolution takes place on comparatively short timescales, strong external influences would be needed to sustain a magnetized eccentric disk in a steady state.

4.5. Implications for TDEs

In TDEs, the tidal gravity of supermassive black holes destroys stars swooping by too close; for main-sequence stars, the critical distance is $\approx 27 (GM/c^2) \times [M/(10^6 M_\odot)]^{-2/3}$, where M is the black hole mass (Ryu et al. 2020). Early analysis suggested that the bound stellar debris would initially be placed on very eccentric orbits with fallback times $t_{fb} \sim 40 \text{ d} \times [M/(10^6 M_\odot)]^{-1/2}$; upon return to the black hole, it would be deposited into a circular accretion flow of radius roughly twice the stellar pericenter (Rees 1988).

Global hydrodynamic simulations (Shiokawa et al. 2015; Steinberg & Stone 2022; Ryu et al. 2023) revealed a very different picture. Over the first few t_{fb} , shocks within the debris transform its shape into an irregular elliptical disk with a mean eccentricity of ~ 0.5 , close to the eccentricity of our simulated disk. The mean semimajor axis of this moderately eccentric disk is only somewhat smaller than that of the debris shortly after disruption, meaning that its orbital period is still $\sim t_{fb}$. During the few months when the disk is forming, the shocks can power optical/ultraviolet (UV) flares with luminosities and timescales roughly matching observed TDE candidates (Piran et al. 2015).

If the debris is threaded with the weak magnetic field of the disrupted star, the MRI in the elliptical disk should grow to nonlinear saturation in ~ 5 to 10 orbits. Thus, MHD stresses grow too slowly to drive much accretion onto the black hole until after the main optical/UV flare has faded. Instead, they could power yearslong low-level emission, releasing at least as much energy over time as the initial flare because accretion onto the black hole should be at least as radiatively efficient as internal debris shocks. This long-term accretion may explain the late-time emission (e.g., van Velzen et al. 2019; Jonker et al. 2020) or rebrightening (e.g., Chen et al. 2022; Liu et al. 2023; Malyali et al. 2023; Wevers et al. 2023) in a number of TDE candidates.

5. CONCLUSIONS

Our earlier work established that the MRI operates in unstratified eccentric disks as vigorously as in circular disks; here we

demonstrate that it does in the presence of vertical gravity as well. Its nonlinear development in a global simulation is qualitatively similar to circular disks, differing only in particulars.

The mean Maxwell stress to pressure ratio α_m is similar to that in circular disks at the order-of-magnitude level: The mean radial flux of azimuthal momentum is outward and has magnitude $\sim 10^{-2}$ times the pressure. Oscillation of the radial velocity between positive and negative causes the Maxwell stress in a small region of the disk to transport angular momentum inward rather than outward.

The strong orbital modulation of vertical gravity creates a brand new channel for reconnection and dissipation, a direct consequence of the strong compression near pericenter. Partly because of this, the magnetic energy is weakened by a factor of ~ 3 over the course of our simulation.

MHD stresses in eccentric disks drive rapid evolution of the radial eccentricity profile, at rates considerably faster than purely hydrodynamic, secular processes. Over only ~ 5 to ~ 10 orbits, MHD stresses transport enough angular momentum to substantially widen the mass distribution over eccentricity and create a strong radial eccentricity gradient with highly eccentric material on the inside.

These MHD effects can strongly influence eccentric disk structure on timescales from a few to many orbits. During the several orbits required to reach nonlinear saturation, they can reshuffle the eccentricity distribution; once the nonlinear stage has been reached, the Maxwell stress created by MRI-driven turbulence can support accretion over longer periods. In particular, in the eccentric disks formed by tidally disrupted stellar debris, the MRI may reach nonlinear saturation in merely ~ 5 to 10 orbits, but this can be long compared to the fallback time; therefore, MRI-driven effects may govern the accretion rate and luminosity on timescales tens of times as long as the initial flare, accounting for the emission years later.

CHC was supported by NSF grant AST-1908042. TP was supported by ERC Advanced Grant ‘‘MultiJets’’ and a grant MP-SCMPS-00001470 from the Simons Foundation to the Simons Collaboration on Extreme Electrodynamics of Compact Sources (SCEECs). JHK was partially supported by NSF grants AST-2009260 and PHY-2110339. The simulation made use of the Extreme Science and Engineering Discovery Environment (XSEDE) Stampede2 at the Texas Advanced Computing Center (TACC) through allocation PHY210115.

Software: Athena++ (White et al. 2016; Stone et al. 2020), NumPy (Harris et al. 2020), SymPy (Meurer et al. 2017), Matplotlib (Hunter 2007)

APPENDIX

A. METRIC COMPONENTS AND CHRISTOFFEL SYMBOLS

The nonzero metric components in orbital coordinates are

$$g_{tt} = -P, \quad (\text{A1})$$

$$g_{\lambda\lambda} = r^2, \quad (\text{A2})$$

$$g_{\lambda\phi} = g_{\phi\lambda} = R^2Q + z^2X, \quad (\text{A3})$$

$$g_{\lambda\zeta} = g_{\zeta\lambda} = z^2/\zeta, \quad (\text{A4})$$

$$g_{\phi\phi} = R^2(1 + Q^2) + z^2X^2, \quad (\text{A5})$$

$$g_{\phi\zeta} = g_{\zeta\phi} = z^2X/\zeta, \quad (\text{A6})$$

$$g_{\zeta\zeta} = z^2/\zeta^2, \quad (\text{A7})$$

$$g^{tt} = -1/P, \quad (\text{A8})$$

$$g^{\lambda\lambda} = (1 + Q^2)/R^2, \quad (\text{A9})$$

$$g^{\lambda\phi} = g^{\phi\lambda} = -Q/R^2, \quad (\text{A10})$$

$$g^{\lambda\zeta} = g^{\zeta\lambda} = -\zeta[1 + Q(Q - X)]/R^2, \quad (\text{A11})$$

$$g^{\phi\phi} = 1/R^2, \quad (\text{A12})$$

$$g^{\phi\zeta} = g^{\zeta\phi} = \zeta(Q - X)/R^2, \quad (\text{A13})$$

$$g^{\zeta\zeta} = \zeta^2[r^2 + z^2(Q - X)^2]/(R^2z^2), \quad (\text{A14})$$

the metric determinant is

$$g = -R^4z^2P/\zeta^2, \quad (\text{A15})$$

and the nonzero Christoffel symbols of the second kind are

$$\Gamma_{t\lambda}^t = \Gamma_{\lambda t}^t = [(\partial_R\Phi)R + (\partial_z\Phi)z]/P, \quad (\text{A16})$$

$$\Gamma_{t\phi}^t = \Gamma_{\phi t}^t = [(\partial_R\Phi)RQ + (\partial_z\Phi)zX]/P, \quad (\text{A17})$$

$$\Gamma_{t\zeta}^t = \Gamma_{\zeta t}^t = (\partial_z\Phi)z/(\zeta P), \quad (\text{A18})$$

$$\Gamma_{tt}^\lambda = \partial_R\Phi/R, \quad (\text{A19})$$

$$\Gamma_{\lambda\lambda}^\lambda = 1, \quad (\text{A20})$$

$$\Gamma_{\phi\phi}^\lambda = -R/\lambda, \quad (\text{A21})$$

$$\Gamma_{\lambda\phi}^\phi = \Gamma_{\phi\lambda}^\phi = 1, \quad (\text{A22})$$

$$\Gamma_{\phi\phi}^\phi = 2Q, \quad (\text{A23})$$

$$\Gamma_{tt}^\zeta = \zeta(\partial_z\Phi/z - \partial_R\Phi/R), \quad (\text{A24})$$

$$\Gamma_{\lambda\zeta}^\zeta = \Gamma_{\zeta\lambda}^\zeta = 1, \quad (\text{A25})$$

$$\Gamma_{\phi\phi}^\zeta = \zeta[R/\lambda - (2Q - X)X + Y], \quad (\text{A26})$$

$$\Gamma_{\phi\zeta}^\zeta = \Gamma_{\zeta\phi}^\zeta = X, \quad (\text{A27})$$

where

$$\Phi(R, z) \equiv -1/(r + 2), \quad (\text{A28})$$

$$r \equiv (R^2 + z^2)^{1/2}, \quad (\text{A29})$$

$$P \equiv 1 + 2\Phi(R, z), \quad (\text{A30})$$

$$Q \equiv e \sin \phi / (1 + e \cos \phi), \quad (\text{A31})$$

$$X \equiv d \ln H_*/d\phi, \quad (\text{A32})$$

$$Y \equiv d^2 \ln H_*/d\phi^2. \quad (\text{A33})$$

B. GRID HEIGHT

The grid height $H_*(\phi)$ controls how the grid stretches in the vertical direction. As mentioned in Section 2.3, we set $H_*(\phi)$ to the scale height of a hydrostatic reference column positioned at some point (λ_*, ϕ) along the characteristic orbit. The goal of this section is to obtain an approximate closed-form expression for H_* ; an exact measurement of the scale height is not needed because H_* does not affect disk physics.

We expand vertical gravity along $\lambda = \lambda_*$ to first order in z as

$$[-\partial_z\Phi]_{\lambda=\lambda_*} \approx -z/[R_*(R_* + 2)^2] = -v_*^2z; \quad (\text{B1})$$

here ν_* is the vertical frequency and $R_* \equiv \lambda_*/(1 + e \cos \phi)$. The vertical density profile of the column is then (e.g., Ryu et al. 2021)

$$\rho_*(\phi, \zeta) \approx \rho_*(\phi, 0) [1 - (\gamma - 1) \zeta^2 / H_*^2]^{1/(\gamma-1)}, \quad (\text{B2})$$

with the scale height of the column given by

$$H_*^2 = 2\gamma K_* \rho_*^{\gamma-1}(\phi, 0) / \nu_*^2. \quad (\text{B3})$$

Equations (B2) and (B3) reduce to their expected forms in the isothermal limit of $\gamma \rightarrow 1$.

Once we have picked a value for the surface density Σ_* of the column, we can solve for $\rho_*(\phi, 0)$ and, through Equation (B3), H_* . In defining the surface density of the column, we break from the common practice of integrating from the midplane to infinity, opting instead for

$$\Sigma_* = \int_0^{(\gamma-1)^{-1/2} H_*} dz \rho_*(\phi, \zeta), \quad (\text{B4})$$

which has the advantage of smoothly connecting to the isothermal surface density when $\gamma \rightarrow 1$. Performing the integral and using Equation (B3) to eliminate $\rho_*(\phi, 0)$, we get

$$\Sigma_* = (\gamma - 1)^{-1/2} (2\gamma K_*)^{-1/(\gamma-1)} {}_2F_1\left(\frac{1}{2}, -(\gamma - 1)^{-1}, \frac{3}{2}; 1\right) \times H_*^{(\gamma+1)/(\gamma-1)} \nu_*^{2/(\gamma-1)}, \quad (\text{B5})$$

where ${}_2F_1$ is the hypergeometric function.

The metric and connection depends on the derivatives of H_* as well. Differentiating Equation (B5) furnishes us with

$$\frac{d^n}{d\phi^n} \ln H_* = -\frac{2}{\gamma + 1} \frac{d^n}{d\phi^n} \ln \nu_*, \quad (\text{B6})$$

where n is a positive integer, and differentiating Equation (B1) yields

$$\frac{d}{d\phi} \ln \nu_* = -\frac{3R_* + 2}{2(R_* + 2)} Q, \quad (\text{B7})$$

$$\frac{d^2}{d\phi^2} \ln \nu_* = -\frac{3R_* + 2}{2(R_* + 2)} \frac{dQ}{d\phi} - \frac{2R_*}{(R_* + 2)^2} Q^2 \quad (\text{B8})$$

with Q from Appendix A.

C. INITIAL ECCENTRIC DISK

The construction of an eccentric disk in approximate force balance begins with an exactly hydrostatic circular torus. This reference torus is described in cylindrical coordinates (R, φ, z) and is governed by five parameters $(\tilde{R}, \tilde{K}, \tilde{\Gamma}, \tilde{\rho}_m, \tilde{q})$. Its density $\tilde{\rho}(R, z)$ and pressure $\tilde{p}(R, z)$ are related by the polytropic equation of state $\tilde{p} = \tilde{K} \tilde{\rho}^{\tilde{\Gamma}}$, and its density maximum is $\tilde{\rho}_m = \tilde{\rho}(\tilde{R}, 0)$. Its orbital velocity follows the shear profile $\tilde{\mathbf{v}}(R) = \tilde{v}_m(R/\tilde{R})^{1-\tilde{q}} \hat{\mathbf{e}}_\varphi$, where the azimuthal velocity at the density maximum is given by $\tilde{v}_m^2 = (R \partial_R \Phi)(\tilde{R}, 0)$. With these stipulations, $\tilde{\rho}$ is the solution to the equation (see also Papaloizou & Pringle 1984; Hawley 2000)

$$\text{constant} = \Phi - \frac{\tilde{v}_\varphi^2}{2(1-\tilde{q})} + \begin{cases} \tilde{K} \frac{\tilde{\rho}}{\tilde{R}^{\tilde{\Gamma}-1}} (\tilde{\rho}^{\tilde{\Gamma}-1} - 1), & \tilde{\Gamma} \neq 1, \\ \tilde{K} \ln \tilde{\rho}, & \tilde{\Gamma} = 1. \end{cases} \quad (\text{C1})$$

We demand $\tilde{R} = \lambda_*$ so that the torus matches the desired initial eccentric disk in characteristic semilatus rectum, and $(\tilde{K}, \tilde{\Gamma}, \tilde{q}) = (9 \times 10^{-6}, 1, 1.55)$ so that the torus is geometrically thin. We also arbitrarily set $\tilde{\rho}_m = 1$. The surface density of such a torus at $R = \tilde{R}$ is

$$\tilde{\Sigma} = \int_0^{\tilde{z}} dz \tilde{\rho}(\tilde{R}, z) \approx 8.30, \quad (\text{C2})$$

the upper limit being the height at which the integrand vanishes.

The circular Newtonian torus tells us how to set up in our simulation a circular GR disk in the weak-gravity limit. We employ eccentric coordinates with $e = 0$ for the initial condition in anticipation of the subsequent conversion of the circular disk to an eccentric one. The vertical scaling of the eccentric coordinate system is governed by a reference column with $(\Sigma_*, K_*) = (\tilde{\Sigma}, \tilde{K})$, which implies $H_*(\phi) \approx 11.9$ for all ϕ . Equations (11)–(13) are used to transform the torus from the cylindrical coordinates in which it is described to eccentric coordinates.

Torus properties must be converted to primitive variables for consumption by the simulation. Density and pressure are directly usable as primitive variables. The Newtonian angular velocity \tilde{v}_φ/R is identified with the GR coordinate velocity u^ϕ/u^t ; together with the constraint $u^\lambda = u^\zeta = 0$ and the normalization condition, the velocity is fully determined.

Once the circular disk is configured on the eccentric coordinate system, it is morphed into an eccentric disk by increasing the eccentricity e of the coordinate system itself. Each cell stays at its coordinate-space location (λ, ϕ, ζ) but shifts to a new physical-space location (R, φ, z) . We use the same reference column as above to define the breathing of the new grid, but now $H_*(\phi)$ is a function of ϕ because different points along the characteristic orbit are at different R_* and experience different levels of vertical gravity. Since we do not touch the grid in coordinate space, we need not interpolate simulation data. We also get vertical motion for free: Grid geometry forces the velocity field to diverge and converge in synchronization with disk expansion and contraction even though $u^\lambda = u^\zeta = 0$.

Two additional tweaks keep the eccentric disk as hydrostatic as possible. Disk reshaping moves material to a different R , breaking the balance between gravitational and centrifugal forces. Restoring that balance involves multiplying u^ϕ of each cell by R^2/λ^2 so that material has the same specific angular momentum as before. Reshaping also changes the disk height, so the mass current along any orbit of constant λ is no longer constant over ϕ . To approximately reinstate mass continuity, we scale ρ in any given column of cells by the same factor so that the surface density of the column equals its value before reshaping. We multiply p by the same factor as well.

An eccentric disk assembled with the aforementioned process is not strictly hydrostatic, but close enough for the study of the MRI. Instead of jumping immediately to the desired eccentricity, one could raise eccentricity stepwise, each step of reshaping followed by a period of relaxation, but we found that this does not yield a quieter disk.

D. INSTANTANEOUS ECCENTRICITY

In Chan et al. (2022), the instantaneous eccentricity \bar{e} of a gas packet in an unstratified disk is defined as the eccentricity of a particle orbit having the same specific energy E and specific

angular momentum L as the gas packet. That definition does not work for a stratified disk because the trajectory of a gas packet does not in general lie in some orbital plane that includes the central object, not even if we smooth out turbulent motion by considering a time-averaged trajectory. This necessitates an alternative approach.

We consider a gas packet at some $(t, \lambda, \phi, \zeta)$. The velocity of the gas packet has physical, cylindrical components u^i , obtained from its contravariant components u^i using equations analogous to Equations (22)–(24). We construct the restriction of this velocity to the midplane, by which we mean a properly normalized velocity in the tangent space of $(t, \lambda, \phi, 0)$ that has the same coordinate velocity as u^μ except in the ζ -direction. Let us denote quantities at $(t, \lambda, \phi, 0)$ by a breve. The construction guarantees a unique solution for the contravariant temporal component \breve{u}^t and the physical, cylindrical components \breve{u}^i of the restricted velocity:

$$\breve{u}^{\hat{R}}/\breve{u}^t = u^{\hat{R}}/u^t, \quad (\text{D1})$$

$$\breve{u}^{\hat{\phi}}/\breve{u}^t = u^{\hat{\phi}}/u^t, \quad (\text{D2})$$

$$\breve{u}^{\hat{z}} = 0, \quad (\text{D3})$$

$$\breve{g}_{tt}\breve{u}^t\breve{u}^t + \breve{u}^{\hat{R}}\breve{u}^{\hat{R}} + \breve{u}^{\hat{\phi}}\breve{u}^{\hat{\phi}} + \breve{u}^{\hat{z}}\breve{u}^{\hat{z}} = -1. \quad (\text{D4})$$

The specific energy and angular momentum of the restricted velocity are $E = \breve{g}_{tt}\breve{u}^t$ and $L = R\breve{u}^{\hat{\phi}}$, respectively; these are the quantities plotted in Figure 6. The instantaneous eccentricity \bar{e} is then obtained in the same way as in Chan et al. (2022):

$$\bar{e}^2 = 1 + (E^2 - 1)L^2/E^4. \quad (\text{D5})$$

REFERENCES

- Balbus, S. A., & Hawley, J. F. 1991, *ApJ*, **376**, 214
— 1998, *RvMP*, **70**, 1
- Bonnell, I. A., & Rice, W. K. M. 2008, *Sci*, **321**, 1060
- Chan, C.-H., Krolik, J. H., & Piran, T. 2018, *ApJ*, **856**, 12
- Chan, C.-H., Piran, T., & Krolik, J. H. 2022, *ApJ*, **933**, 81
- Chen, J.-H., Dou, L.-M., & Shen, R.-F. 2022, *ApJ*, **928**, 63
- Dewberry, J. W., Latter, H. N., Ogilvie, G. I., & Fromang, S. 2020, *MNRAS*, **497**, 451
- Eracleous, M., Livio, M., Halpern, J. P., & Storchi-Bergmann, T. 1995, *ApJ*, **438**, 610
- Gammie, C. F., McKinney, J. C., & Tóth, G. 2003, *ApJ*, **589**, 444
- Gänsicke, B. T., Marsh, T. R., Southworth, J., & Rebassa-Mansergas, A. 2006, *Sci*, **314**, 1908
- Goodman, J., & Xu, G. 1994, *ApJ*, **432**, 213
- Guillochon, J., Manukian, H., & Ramirez-Ruiz, E. 2014, *ApJ*, **783**, 23
- Harris, C. R., Millman, K. J., van der Walt, S. J., et al. 2020, *Natur*, **585**, 357
- Hawley, J. F. 2000, *ApJ*, **528**, 462
- Hawley, J. F., & Balbus, S. A. 1991, *ApJ*, **376**, 223
- Hawley, J. F., Gammie, C. F., & Balbus, S. A. 1995, *ApJ*, **440**, 742
- Hawley, J. F., Guan, X., & Krolik, J. H. 2011, *ApJ*, **738**, 84
- Hawley, J. F., & Krolik, J. H. 2002, *ApJ*, **566**, 164
- Hawley, J. F., Richers, S. A., Guan, X., & Krolik, J. H. 2013, *ApJ*, **772**, 102
- Hirose, S., Krolik, J. H., & Stone, J. M. 2006, *ApJ*, **640**, 901
- Hunter, J. D. 2007, *CSE*, **9**, 90
- Jacquemin-Ide, J., Rincon, F., Tchekhovskoy, A., & Liska, M. 2023, arXiv: 2311.00034
- Jonker, P. G., Stone, N. C., Generozov, A., van Velzen, S., & Metzger, B. 2020, *ApJ*, **889**, 166
- Kato, S. 1978, *MNRAS*, **185**, 629
- Lazarian, A., & Vishniac, E. T. 1999, *ApJ*, **517**, 700
- Liu, F. K., Zhou, Z. Q., Cao, R., Ho, L. C., & Komossa, S. 2017, *MNRAS*, **472**, L99
- Liu, Z., Malyali, A., Krumpke, M., et al. 2023, *A&A*, **669**, A75
- Lubow, S. H. 1991, *ApJ*, **381**, 259
- Lynch, E. M., & Ogilvie, G. I. 2021a, *MNRAS*, **500**, 4110
— 2021b, *MNRAS*, **501**, 5500
- Lyubarskij, Y. E., Postnov, K. A., & Prokhorov, M. E. 1994, *MNRAS*, **266**, 583
- Malyali, A., Liu, Z., Rau, A., et al. 2023, *MNRAS*, **520**, 3549
- Meurer, A., Smith, C. P., Paprocki, M., et al. 2017, *PeerJ Comput. Sci.*, **585**, e103
- Murray, C. D., & Dermott, S. F. 1999, *Solar System Dynamics* (Cambridge: Cambridge University Press)
- Ogilvie, G. I. 2001, *MNRAS*, **325**, 231
- Ogilvie, G. I. 2008, *MNRAS*, **388**, 1372
- Ogilvie, G. I., & Barker, A. J. 2014, *MNRAS*, **445**, 2621
- Papaloizou, J. C. B. 2005a, *A&A*, **432**, 743
— 2005b, *A&A*, **432**, 757
- Papaloizou, J. C. B., & Pringle, J. E. 1984, *MNRAS*, **208**, 721
- Piran, T., Svirski, G., Krolik, J., Cheng, R. M., & Shiokawa, H. 2015, *ApJ*, **806**, 164
- Rees, M. J. 1988, *Natur*, **333**, 523
- Ryu, T., Krolik, J., & Piran, T. 2021, *ApJ*, **920**, 130
- Ryu, T., Krolik, J., Piran, T., & Noble, S. C. 2020, *ApJ*, **904**, 98
- Ryu, T., Krolik, J., Piran, T., Noble, S. C., & Avara, M. 2023, *ApJ*, **957**, 12
- Sandoval, A., Riquelme, M., Spitkovsky, A., & Bacchini, F. 2023, arXiv: 2308.12348
- Shakura, N. I., & Sunyaev, R. A. 1973, *A&A*, **24**, 337
- Shiokawa, H., Krolik, J. H., Cheng, R. M., Piran, T., & Noble, S. C. 2015, *ApJ*, **804**, 85
- Statler, T. S. 2001, *AJ*, **122**, 2257
- Steinberg, E., & Stone, N. C. 2022, arXiv: 2206.10641
- Stone, J. M., Tomida, K., White, C. J., & Felker, K. G. 2020, *ApJS*, **249**, 4
- Svirski, G., Piran, T., & Krolik, J. 2017, *MNRAS*, **467**, 1426
- Teyssandier, J., & Ogilvie, G. I. 2016, *MNRAS*, **458**, 3221
- Trevascus, D., Price, D. J., Nealon, R., et al. 2021, *MNRAS*, **505**, L21
- Tucker, M. A., Shappee, B. J., Hinkle, J. T., et al. 2021, *MNRAS*, **506**, 6014
- Van Velzen, S., Stone, N. C., Metzger, B. D., et al. 2019, *ApJ*, **878**, 82
- Wevers, T., Coughlin, E. R., Pasham, D. R., et al. 2023, *ApJL*, **942**, L33
- White, C. J., Stone, J. M., & Gammie, C. F. 2016, *ApJS*, **225**, 22
- Whitehurst, R. 1988, *MNRAS*, **232**, 35
- Wissing, R., Shen, S., Wadsley, J., & Quinn, T. 2022, *A&A*, **659**, A91
- Zier, O., & Springel, V. 2022, *MNRAS*, **517**, 2639